Supplementary material for:

Evaluating Thermo-Optical and Aerosol Mass Spectrometry derived Organic Carbon: Seasonal and Site-Specific Discrepancies

Shubhi Arora[1], Laurent Poulain[1], Radek Lhotka[2], Jaroslav Schwarz[2], Petr Vodička[2], Saliou Mbengue[3], Naděžda Zíková[2], Jakub Ondráček[2], Petra Pokorná[2], Vladimír Ždímal[2*], Hartmut Herrmann[1*]

1: Leibniz Institute for Tropospheric Research (TROPOS), Permoserstr. 15, 04318 Leipzig, Germany
2: Institute of Chemical Process Fundamentals CAS, of the Czech Academy of Sciences, Prague, 16500, Czech Republic
3: Global Change Research Institute of the Czech Academy of Sciences, Brno, 60300, Czech Republic

***: Co-corresponding authors**

Table S1: Mean OM:OC ratios derived from eqs. (1) and (2), ratios of AMS-derived OM to OC from offline and online TOT analysis, elemental O:C, and f_{44} at MEL, FRY, and NAOK during winter. Values in parentheses for MEL represent OM:OC ratios obtained from HR (PIKA) analysis.

Season	Station	OM: OC	OM_{AMS}: $OC_{Offline}$	OM_{AMS}: OC_{Online}	O:C	f44
Winter	MEL	2.64 (2.05)	0.57	-	0.72	0.16
	FRY	2.53	0.35	0.53	1.06	0.24
	NAOK	2.34	1.54	1.66	0.91	0.19
Summer	MEL	2.57 (1.93)	1.25	1.93	0.67	0.14
	FRY	2.13	1.54	2.28	0.74	0.15
	NAOK	2.81	1.72	-	0.85	0.18

Text S1: eBC and BrC

The eBC mass concentration at 880 nm was directly obtained from the aethalometer (AE33, Magee Scientific, Slovenia), which reports eBC using the manufacturer's default mass absorption cross section (MAC) of 7.77 $m^2\ g^{-1}$. No site-specific corrections were applied. The BrC mass concentration was estimated in two main steps following the Ångström exponent approach (Lack

and Langridge, 2013; Massabò et al., 2015). First, the absorption attributed to BrC at 370 nm was isolated from the total absorption using an absorption Ångström exponent (AAE) of 1 for eBC. Second, the derived BrC absorption was converted to mass concentration using site-specific MAC values based on concurrent OA measurements according to Mosquera et al. (2024). The MAC values (at 370 nm) were 4.5, 7.4, and 1.3 $m^2\ g^{-1}$ in winter and 0.3, 0.4, and 0.3 $m^2\ g^{-1}$ in summer for MEL, FRY, and NAOK, respectively. At a given wavelength λ_1, total absorption ($b_{a\beta s}$, total) can be expressed as the sum of eBC and BrC contributions:

$$b_{abs,\ Total}(\lambda_1) = b_{abs,\ BrC}(\lambda_1) + b_{abs,\ eBC}(\lambda_1) \quad (1)$$

The eBC absorption Ångström exponent (AAE_{eBC}) for two wavelengths λ_1 and λ_2 ($\lambda_2 > \lambda_1$) follows:

$$\frac{b_{abs,\ eBC}(\lambda_1)}{b_{abs,\ eBC}(\lambda_2)} = \left(\frac{\lambda_1}{\lambda_2}\right)^{-\mathrm{AAE}_{eBC}} \quad (2)$$

Assuming negligible BrC absorption at 880 nm (λ_2) and using an $AAE_eBC = 1$, eBC absorption at 370 nm can be estimated as:

$$b_{abs,\ eBC}(370\ nm) = b_{abs,\ eBC}(880\ nm)\left(\frac{370}{880}\right)^{-1} \quad (3)$$

The BrC absorption coefficient at 370 nm is then obtained from:

$$b_{abs,\ BrC}(370\ nm) = b_{abs,\ Total}(370\ nm) - b_{abs,\ eBC}(880\ nm)\left(\frac{370}{880}\right)^{-1}. \quad (4)$$

BrC absorption at 370 nm was converted to mass concentration using site-specific MAC_{OA} values determined following Mosquera et al. (2024). The MAC_{oa} values, obtained from the slope of BrC absorption versus OA mass concentration, were 4.5, 7.4, and 1.3 $m^2\ g^{-1}$ in winter and 0.3, 0.4, and 0.3 $m^2\ g^{-1}$ in summer for MEL, FRY, and NAOK, respectively. The resulting BrC mass concentration was derived as the ratio of BrC absorption to the corresponding $MAC_{OA.}$ eBC mass was directly taken from the AE33 output based on the default MAC of 7.77 $m^2\ g^{-1}$ at 880 nm.

Table S2. Mean values of OC, EC, and TC from online and offline TOT analysis, eBC and BrC from aethalometer measurements, the OA:eBC ratio, and $MAC_{BrC,370}$ at the three stations.

Season	**Winter**			**Summer**		
Station	**MEL**	**FRY**	**NAOK**	**MEL**	**FRY**	**NAOK**
OC_online	-	2.71 ± 1.74	4.81 ± 2.81	1.82 ± 0.95	1.75 ± 0.76	-
OC_offline	3.12 ± 2.05	3.81 ± 2.36	4.79 ± 3.62	2.76 ± 1.20	2.40 ± 1.08	2.54 ± 1.08
EC_online	-	0.50 ± 0.44	0.63 ± 0.51	0.11 ± 0.10	0.14 ± 0.15	-
EC_offline	0.45 ± 0.32	0.44 ± 0.29	0.41 ± 0.27	0.16 ± 0.06	0.17 ± 0.07	0.16 ± 0.08
TC_online	-	3.21 ± 2.15	5.43 ± 3.25	1.94 ± 1.02	1.89 ± 0.85	-
TC_offline	3.59 ± 2.35	4.24 ± 2.63	5.19 ± 3.86	2.92 ± 1.25	2.60 ± 1.16	2.88 ± 2.10
eBC (conc)	0.76 ± 0.61	0.74 ± 0.56	1.24 ± 0.97	0.27 ± 0.20	0.44 ± 0.50	0.26 ± 0.17
BrC (conc)	1.13 ± 1.10	1.29 ± 1.26	2.26 ± 2.87	0.91 ± 1.77	1.01 ± 1.52	0.80 ± 0.50
OA:eBC	3.06 ± 0.99	1.12 ± 0.56	10.21 ± 5.41	21.97 ± 9.14	12.02 ± 3.82	18.44 ± 4.36

$MAC_{BrC,370}$	5.06 ± 4.75	12.21 ± 7.84	1.61 ± 0.81	0.58 ± 0.41	0.51 ± 0.31	0.54 ± 0.39

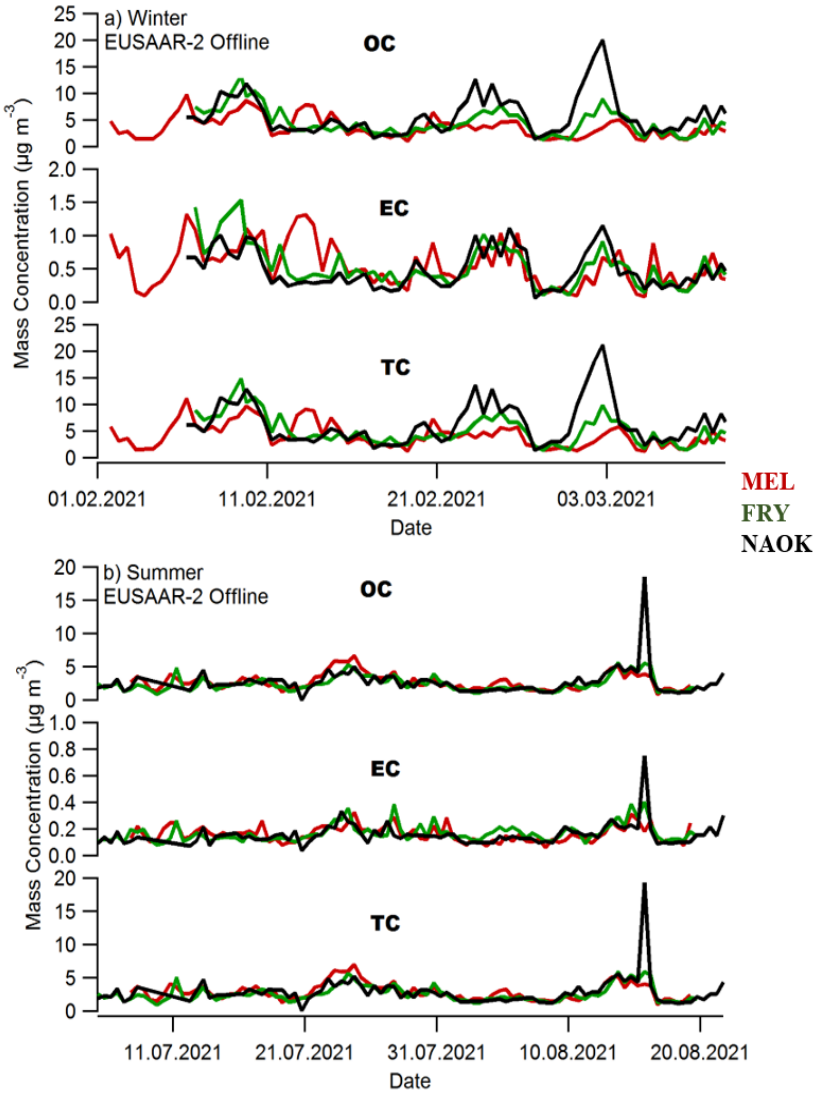

Figure S1: Time series of $OC_{Offline}$, $EC_{Offline}$ and $TC_{Offline}$ concentrations during (a) winter and (b) summer campaigns at MEL, FRY, and NAOK. Measurements are shown as 12-hour averages for $PM_{2.5}$ filter samples.

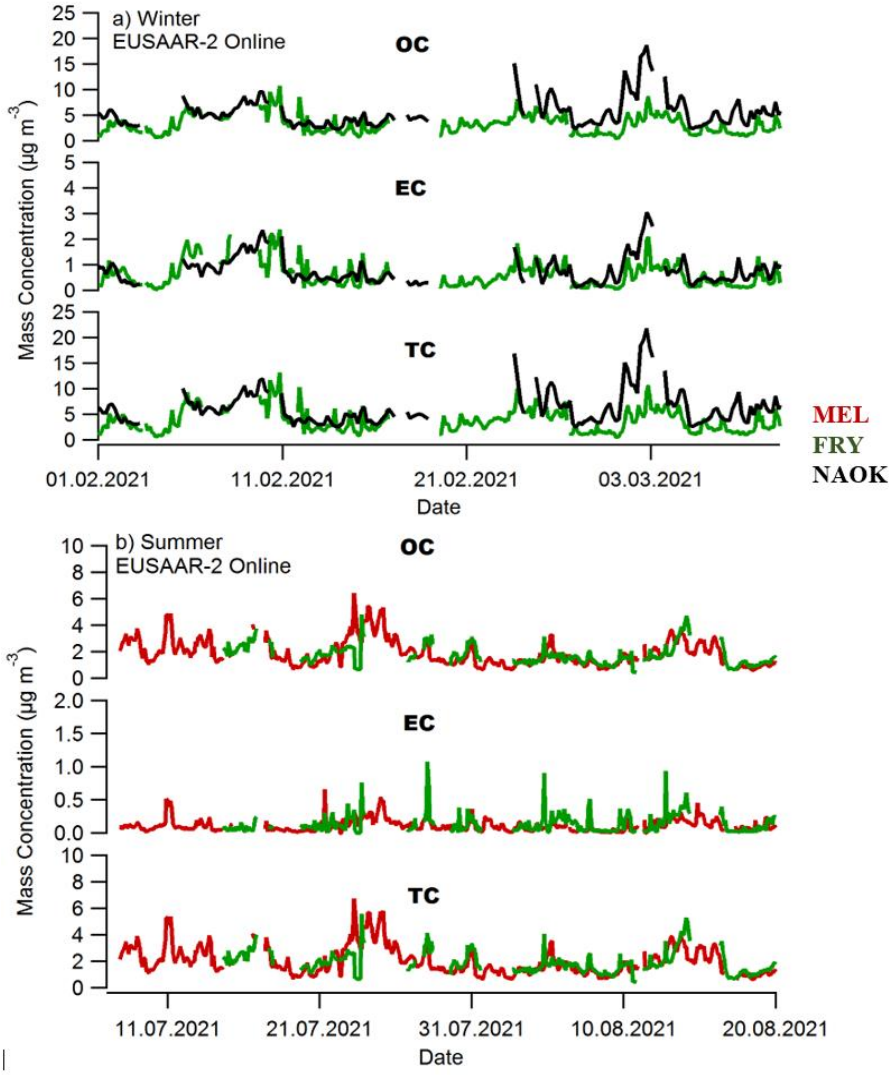

Figure S2: Time series of OC_{Online}, EC_{Online} and TC_{Online} concentrations during (a) winter and (b) summer campaigns at MEL, FRY, and NAOK. Measurements are shown as 12-hour averages for $PM_{2.5}$ filter samples.

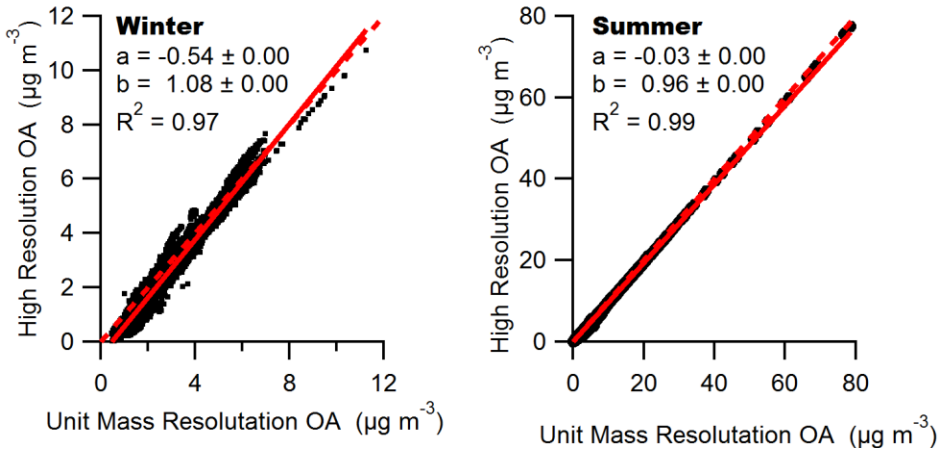

Figure S3: Intercomparison of organic carbon between UMR and HR during winter and summer at MEL using HR-ToF-AMS

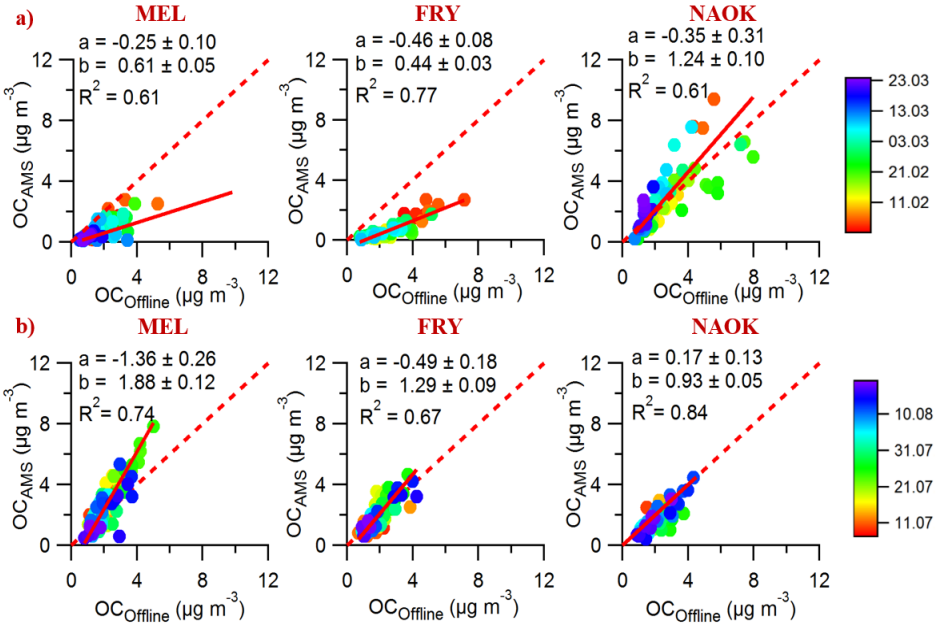

Figure S4: Comparison of OC_{AMS} with $OC_{Offline}$ measurements after applying pyrolysis corrections in a) winter (top) and b) summer (bottom) at MEL, FRY, and NAOK. Solid red lines show orthogonal distance regression fits, and dashed red lines indicate the 1:1 relationship. Slopes (b), intercepts (a), and R^2 values are provided for each site. Course of time is in color for each season.

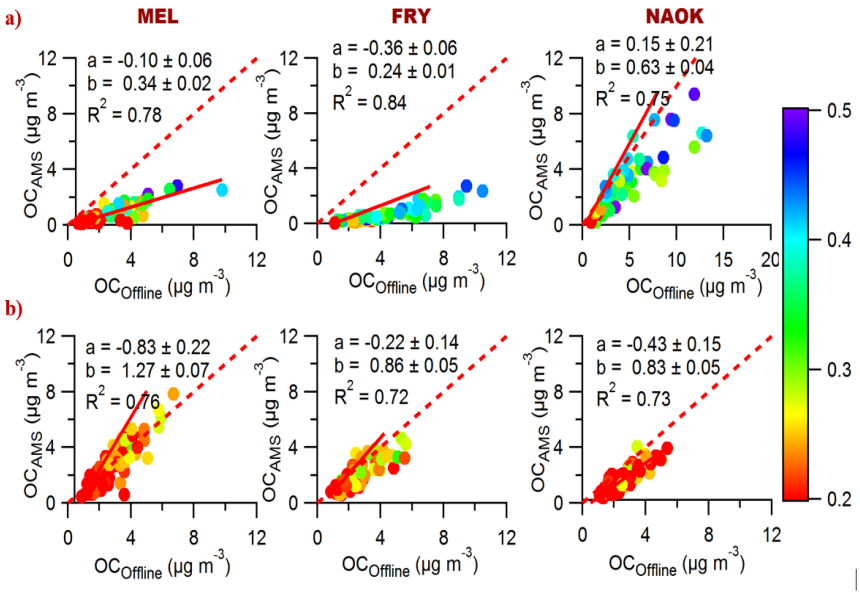

Figure S5: Comparison of OC_{AMS} with $OC_{Offline}$ measurements as a function of PC/TC in a) winter (top) and b) summer (bottom) at MEL, FRY, and NAOK . Solid red lines show orthogonal distance regression fits, and dashed red lines indicate the 1:1 relationship. Slopes (b), intercepts (a), and R^2 values are provided for each site. Data points are colored according to the PC/TC ratio, as indicated by the color bar

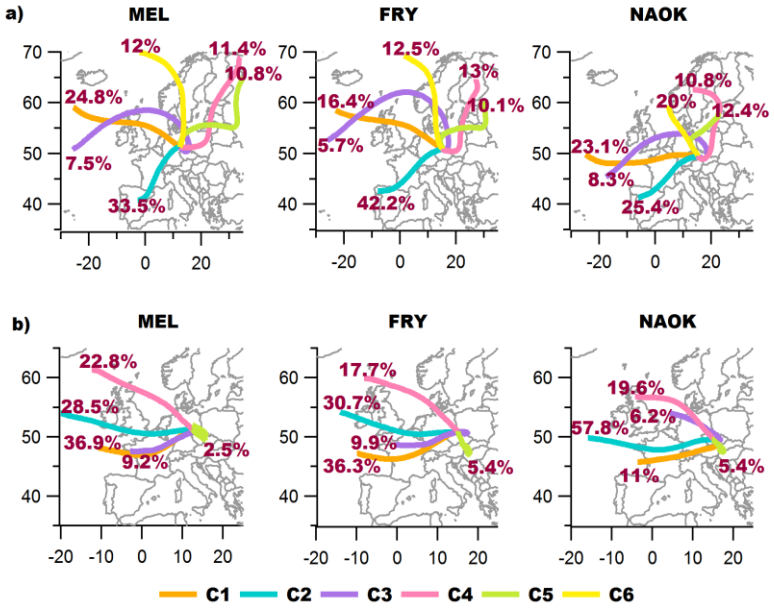

Figure S6: Trajectory clustering for the three stations identified a) six winter (C1W-C6W) and b) five summer (C1S-C5S) back trajectory clusters. In winter, clusters C1W and C6W represented marine inflow from the North Atlantic and Norwegian Sea, whereas C2W, C4W, and C5W traced continental transport from Western, Northern, and Eastern Europe, respectively. These continental clusters were associated with elevated PM_1, OA, and eBC concentrations due to advection of

combustion-influenced air from industrialized regions in Central and Eastern Europe. Cluster C3W, passing Scandinavia, showed lower mass loadings consistent with cleaner marine influence. In summer, air masses were largely marine (≈ 85-90 % of trajectories), with C1S and C2S originating from the North Atlantic and dominating at all stations. Continental clusters C3S and C4S (from France and the North Sea, respectively) showed modest mass contributions, while C5S reflected stagnant conditions over Central Europe with the highest PM and carbonaceous aerosol concentrations. Overall, winter was characterized by stronger continental transport contrasts among sites, whereas summer showed more uniform, regionally mixed air masses dominated by marine and biogenic influence (Arora et al., 2025).

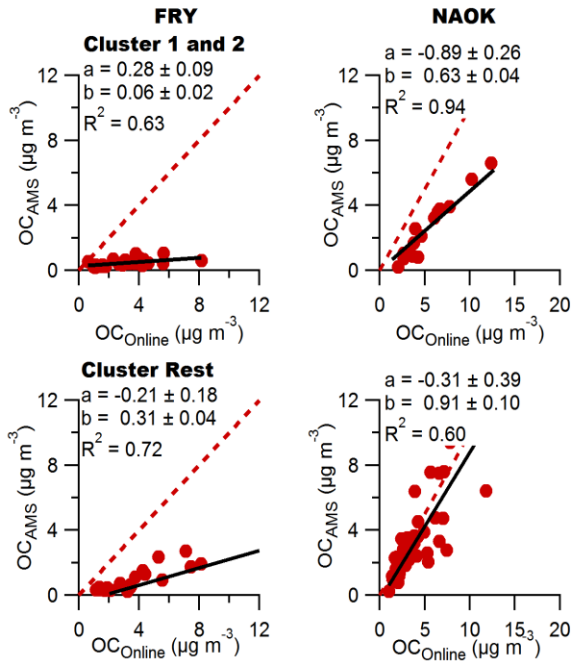

Figure S7: Comparison of organic carbon (OC) concentrations measured by AMS-derived OC (PM_1) and online Sunset thermo-optical OC, illustrating the impact of clusters. Top panels represent Clusters 1 and 2, and bottom panels represent the rest of the clusters (3, 4, 5, and 6) for FRY, and NAOK stations during winter. The dashed red line indicates a 1:1 relationship.

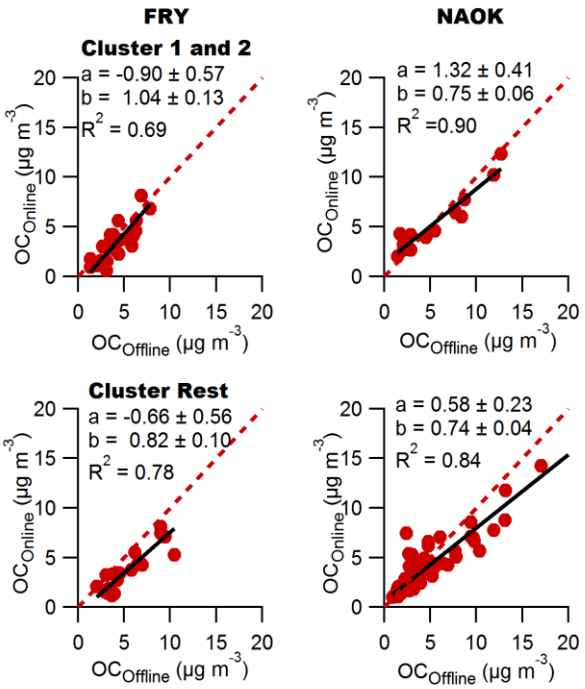

Figure S8: Comparison of OC_{Online} with $OC_{Offline}$ concentrations during winter at FRY and NAOK separated by air mass clusters. Top panels show periods dominated by long-range transport clusters 1 and 2; bottom panels show the remaining clusters. Solid black lines represent orthogonal distance regression fits; dashed red lines indicate the 1:1 relationship. Slopes (b), intercepts (a), and R^2 values

Table S3: Average Wind Speed and temperature for each cluster during winter at the three stations.

	C1W	C2W	C3W	C4W	C5W	C6W
Average Wind Speed						
MEL	2.62	2.5	2.28	4.01	1.95	1.67
FRY	2.61	5.05	2.3	5.44	2.01	2.79
NAOK	3.34	2.83	2.25	2.37	2.8	2.75
Average Temperature						
MEL	2.24	4.27	1.06	-7.29	-10.3	-8.6
FRY	1.71	5.46	3.31	-2.41	-9.77	-2.76
NAOK	2.8	5.04	0.682	-3.26	-8.51	-2.13

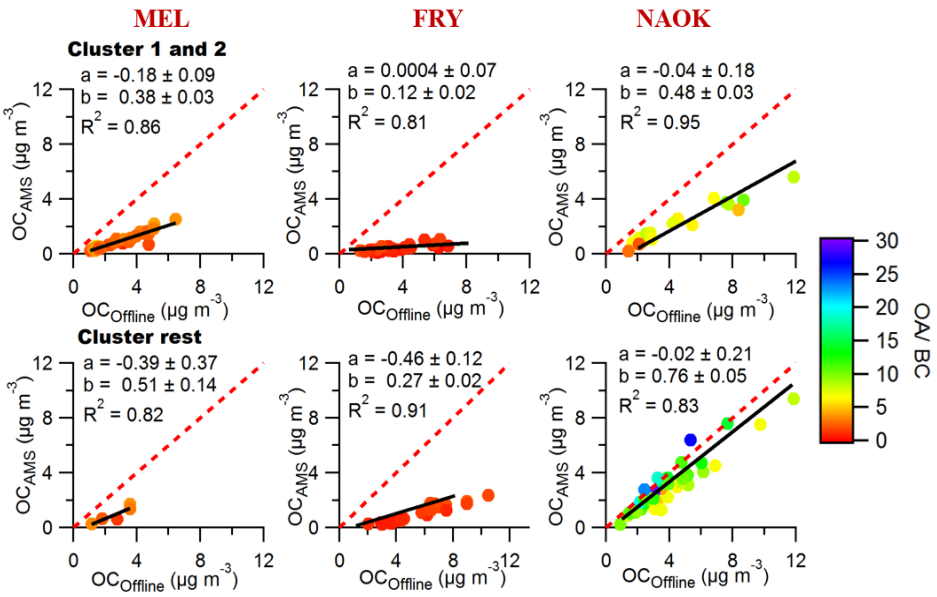

Figure S9: Comparison of AMS-derived OC (PM_1) with offline OC ($PM_{2.5}$) concentrations during winter, separated by air mass origin clusters in a) winter (top) and b) summer (bottom) at MEL, FRY, and NAOK as a function of OA:eBC. The top panels show Clusters 1 and 2, while the bottom panels represent the remaining clusters (C3–C6). Regression parameters (slope *b*, intercept *a*, and R^2) are given for each site. The dashed red line indicates the 1:1 relationship, and the solid black line represents the orthogonal distance regression fit.

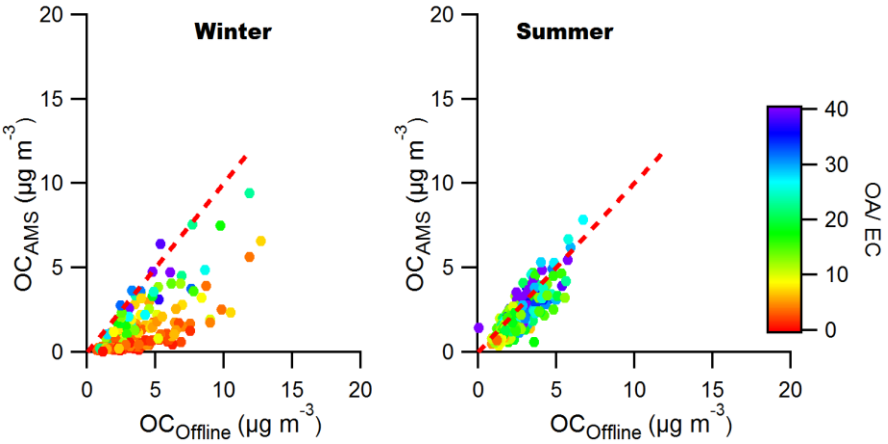

Figure S10: Comparison of OC concentrations measured by AMS-derived OC (PM_1) and offline Sunset OC thermal-optical ($PM_{2.5}$) as a function of OA:EC ratio during winter and summer at MEL, FRY, and NAOK

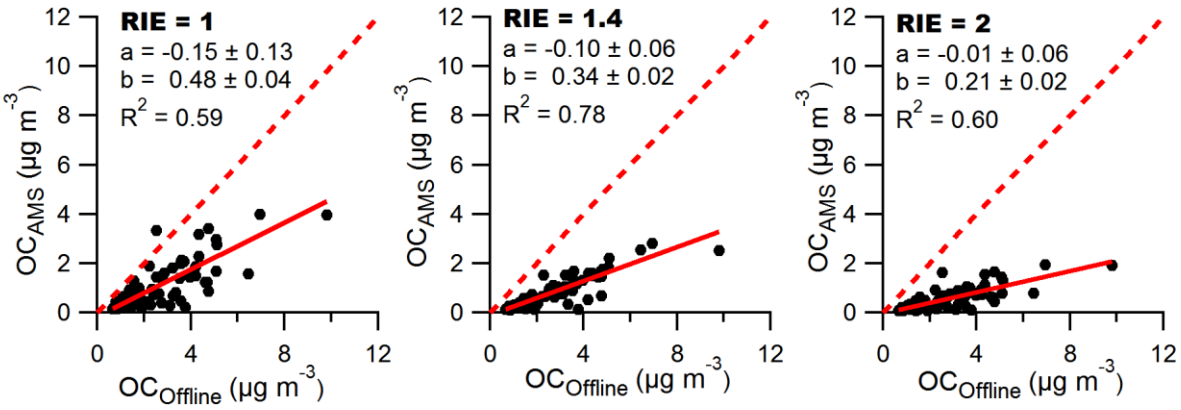

Figure S11: Sensitivity analysis of the impact of varying the relative ionization efficiency (RIE) on the agreement between OC_{AMS} and $OC_{Offline}$ at MEL during winter. Panels show orthogonal distance regression fits (solid red lines) for RIE values of 1, 1.4 (default), and 2, with dashed red lines indicating the 1:1 relationship. Despite changes in RIE, slopes (b) and R^2 values demonstrate only minor improvements in correlation, indicating that RIE adjustments alone cannot account for the discrepancies between AMS and thermal-optical OC measurements.

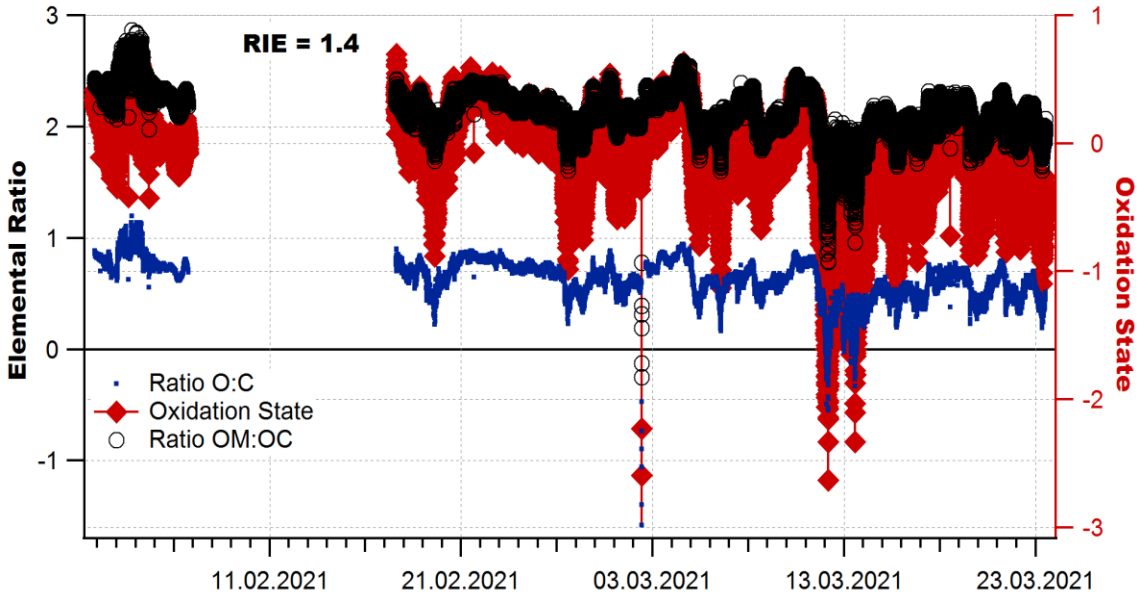

Figure S12: Time series of elemental ratios for organic aerosol measured by HR-ToF-AMS at MEL during winter, assuming RIE = 1.4. Shown are the O:C ratio (blue squares, left y-axis), OM:OC ratio (black circles, left y-axis), and calculated oxidation state (red diamonds, right y-axis). The predominance of oxidation states between –1 and 0 indicates fresh, less-oxidized primary organic aerosol (POA), consistent with elevated contributions from combustion sources and highlighting potential challenges in accurate OC quantification using standard RIE values.

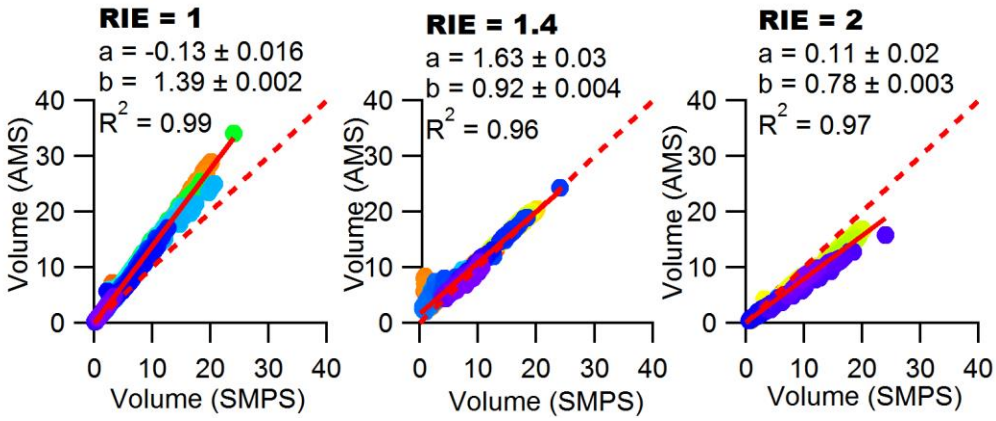

Figure S13: Mass closure plots comparing AMS-derived aerosol volume to SMPS volume at MEL winter under different organic RIE assumptions (RIE=1, 1.4, 2). Slopes (b) show that deviations from the default RIE=1.4 (b=0.92) cause substantial overestimation (b=1.39) or underestimation (b=0.78) of aerosol volume by AMS.

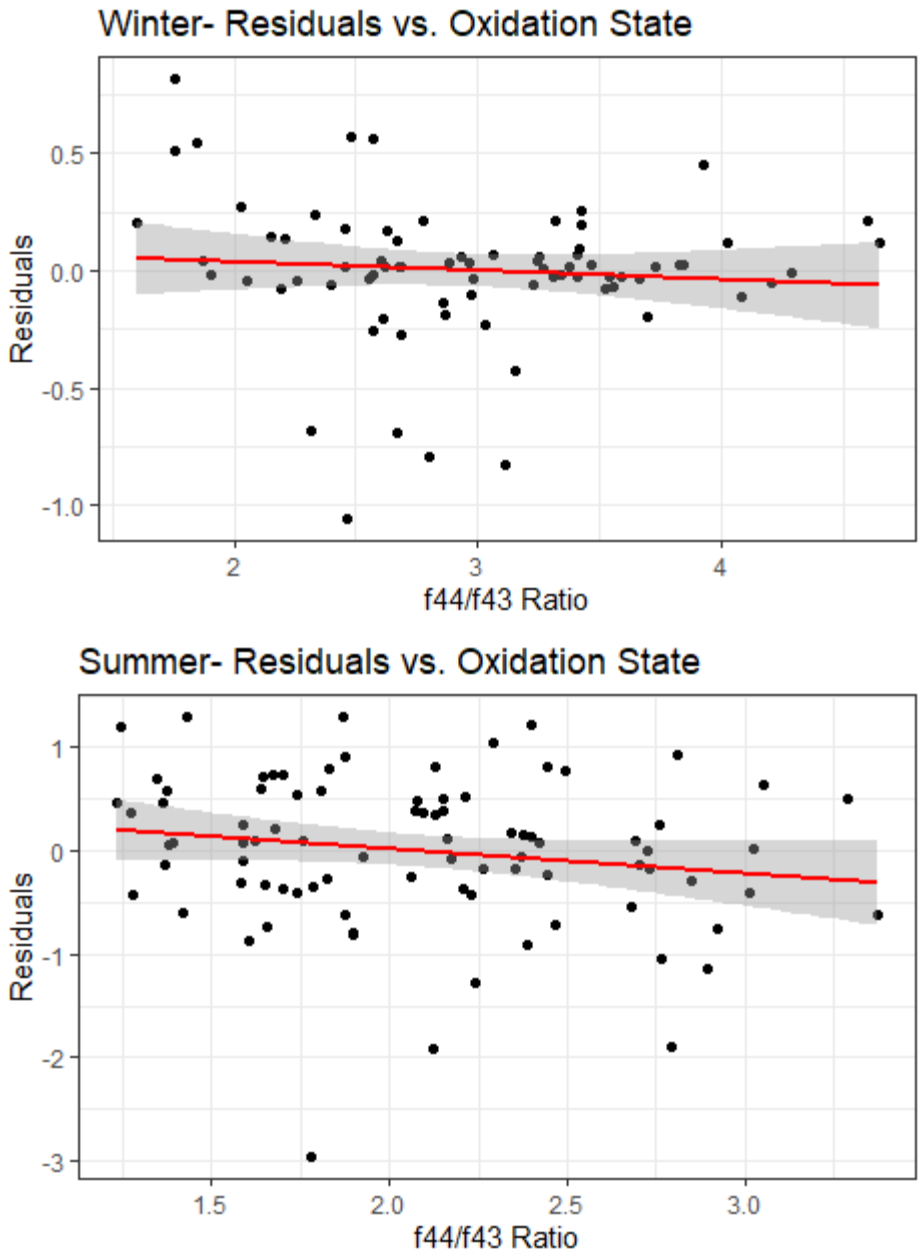

Figure S14: Scatter plots show residuals of the linear regression between OC AMS and OC Offline as a function of the f44/f43 ratio for (a) winter and (b) summer periods. Each point represents a measurement interval, with the red line indicating a linear fit and shaded 95% confidence intervals. A weak, non-significant negative correlation was observed in both seasons (summer: r = –0.171, p = 0.115; winter: r = –0.086, p = 0.461), indicating that variations in oxidation state did not significantly influence the agreement between AMS-derived and thermal-optical OC measurements.

For each measurement interval, OC AMS residuals were calculated as the difference between the measured OC AMS and the fitted OC AMS value from a linear regression of OC AMS on OC Offline (OC AMS fitted = a + b × OC Offline). The oxidation proxy was determined as the f44/f43

ratio from AMS data. Pearson correlation analysis was performed between the residuals and the f44/f43 ratio, with significance assessed using a two-tailed test. Scatter plots of residuals versus f44/f43 were generated with linear fits and 95% confidence intervals.

References

Huang, W., Wu, C., Gao, L., Gramlich, Y., Haslett, S. L., Thornton, J., Lopez-Hilfiker, F. D., Lee, B. H., Song, J., Saathoff, H., Shen, X., Ramisetty, R., Tripathi, S. N., Ganguly, D., Jiang, F., Vallon, M., Schobesberger, S., Yli-Juuti, T., and Mohr, C.: Variation in chemical composition and volatility of oxygenated organic aerosol in different rural, urban, and mountain environments, Atmos. Chem. Phys., 24, 2607–2624, https://doi.org/10.5194/acp-24-2607-2024, 2024.

Lack, D. A. and Langridge, J. M.: On the attribution of black and brown carbon light absorption using the Ångström exponent, Atmos. Chem. Phys., 13, 10535–10543, https://doi.org/10.5194/acp-13-10535-2013, 2013.

Massabò, D., Caponi, L., Bernardoni, V., Bove, M. C., Brotto, P., Calzolai, G., Cassola, F., Chiari, M., Fedi, M. E., Fermo, P., Giannoni, M., Lucarelli, F., Nava, S., Piazzalunga, A., Valli, G., Vecchi, R., and Prati, P.: Multi-wavelength optical determination of black and brown carbon in atmospheric aerosols, Atmos. Environ., 108, 1–12, https://doi.org/10.1016/j.atmosenv.2015.02.058, 2015.

Moschos, V., Dzepina, K., Bhattu, D., Lamkaddam, H., Casotto, R., Daellenbach, K. R., Canonaco, F., Rai, P., Aas, W., Becagli, S., Calzolai, G., Eleftheriadis, K., Moffett, C. E., Schnelle-Kreis, J., Severi, M., Sharma, S., Skov, H., Vestenius, M., Zhang, W., and El Haddad, I.: Equal abundance of summertime natural and wintertime anthropogenic Arctic organic aerosols, Nat. Geosci., 15, 196–202, https://doi.org/10.1038/s41561-021-00891-1, 2022.

Qi, L., Vogel, A. L., Esmaeilirad, S., Cao, L., Zheng, J., Jaffrezo, J.-L., Fermo, P., Kasper-Giebl, A., Daellenbach, K. R., Chen, M., Ge, X., Baltensperger, U., Prévôt, A. S. H., and Slowik, J. G.: A 1-year characterization of organic aerosol composition and sources using an extractive electrospray ionization time-of-flight mass spectrometer (EESI-TOF), Atmos. Chem. Phys., 20, 7875–7893, https://doi.org/10.5194/acp-20-7875-2020, 2020.